Chapter 1
Electron Microscopy and Microanalysis for Wear Surface Characterization

Focused Ion-Beam, Electron Backscattered Diffraction and Transmission Electron Microscopy

Joseph R. Michael, Paul G. Kotula and Somuri V. Prasad

Abstract Wear surface analysis, specifically in the subsurface regions, is essential for understanding the fundamental mechanisms of friction and material removal during wear. The advent of focused ion-beam systems (combined scanning electron and focused ion-beam microscopes) has made it possible to prepare site-specific cross sections of wear surfaces for scanning electron microscopy, electron backscattered diffraction, transmission electron microscopy, and X-ray microanalysis. During the past decade, these state-of-the-art electron microscopy techniques are being increasingly used to characterize wear-induced changes to microstructures and crystallographic textures.

1.1 Introduction

Wear damage is typically initiated in the subsusurface regions of the contacting sliding surfaces before it is fully manifested on the top surface, see Fig. 1.1. In metallic alloys, sliding contact results in plastic deformation, which often leads to recrystallization and development of crystallographic texture [1]. In the case of brittle materials, microscopic fracture events in the subsurface regions are the principal source

J. R. Michael · P. G. Kotula · S. V. Prasad (✉)
Sandia National Laboratories, Albuquerque, NM 87185-0886, USA
e-mail: svprasa@sandia.gov

J. R. Michael
e-mail: jrmicha@sandia.gov

P. G. Kotula
e-mail: pgkotul@sandia.gov

© Springer Nature Switzerland AG 2018

M. Dienwiebel and M.-I. De Barros Bouchet (eds.), *Advanced Analytical Methods in Tribology*, Microtechnology and MEMS,
https://doi.org/10.1007/978-3-319-99897-8_1

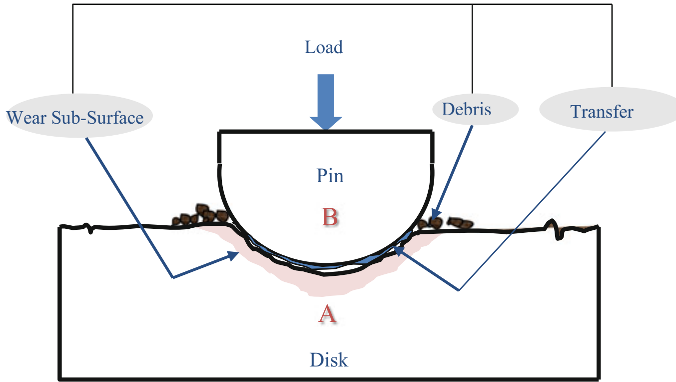

Fig. 1.1 Schematic illustration of the cross-section of a typical pin-on-disk wear system showing the subsurfaces

for wear damage [2]. Amorphous to crystalline transitions in the subsurface regions of transition metal dichalcogenide solid lubricating thin films (e.g., MoS_2, WS_2), with basal planes aligning in the sliding direction, and formation of transfer films on the counterface have been well documented [3]. Now it is widely acknowledged that a fundamental understanding of the friction-induced microstructural changes in the subsurface regions is essential for analyzing the wear mechanisms.

Up until the 1960s, wear surface analysis has primarily relied on visualization of wear damage from optical microscopy of wear surfaces. Metallographic cross-sections were sometimes prepared by cutting the sample obliquely to enhance the vertical magnification relative to the horizontal one. Like in the case of focused ion beam milling, which will be described in the later sections, it is necessary to protect the surface from damage from metallographic sample preparation. This is typically done by electroplating the surface with a metal of similar hardness. Using this technique, Moore [4] resolved the features indicative of plastic deformation and work hardening underneath the finely scratched, machined and lapped surfaces of metals (see also Bowden and Tabor [5]).

The advent of scanning and transmission electron microscopes in the 1960s, provided a powerful tool to the tribologists with high resolution imaging for visualizing the surface features, orders of magnitude higher than the optical microscopy [6]. Simultaneously, elemental and chemical analyses of the wear surfaces were made possible by X-ray and electron spectroscopy [7], while electron diffraction in the transmission electron microcopy enabled the determination of the crystal structures. However, specimen preparation for cross-sectional analyses remained a challenging task. SEM examination of subsurfaces continued to rely on dicing followed by conventional metallographic sample preparation techniques. Earlier research on cross-sectional transmission electron microscopy (TEM) of wear surfaces did not gain widespread application due to the difficulty in preparing the TEM samples by conventional techniques, which involved core drilling or dicing by diamond saw,

grinding, electropolishing and dimpling [8, 9]. These steps are not only cumbersome and time consuming, but also are inadequate in locating the substructures in specific locations on the wear surface. This chapter will first highlight the application of modern focused ion beam (FIB) microscopy techniques for visualization of friction-induced deformation in the subsurfaces as well as the preparation of TEM samples in site-specific locations on a wear surface. This will be followed by specific examples from our recent research on the application of electron backscatter diffraction (EBSD) and high-resolution TEM for analyzing the friction and wear mechanisms in nanocrystalline metals and transition metal dichalcogenides.

1.2 Focused Ion Beam Preparation and Scanning Electron Microscopy

1.2.1 Focused Ion Beam (FIB) Preparation of Samples

The development of the combined focused ion beam/scanning electron microscope platforms (referred to as FIB/SEM) is possibly one of the most important developments that has enabled an improved understanding of sub-surface microstructural changes due to wear [11, 12]. The FIB/SEM at the simplest level is the combination of a high-resolution imaging tool (SEM) with a precision machining tool (FIB). This combination has turned out to be extremely powerful and has enabled the production of site specific samples for SEM imaging and other analytical techniques, such as transmission electron microscopy (TEM), surface analysis, micromechanical testing and many other analytical methods.

There are now two main ion sources for FIB tools, the liquid metal ion source (LMIS) and the plasma source. The most common source is a LMIS that typically produces a Ga+ ion beam that is used to micromachine via sputtering of selected regions of the sample. The LMIS equipped FIB allows small ion beams to be formed that are very useful for the preparation of samples that are on the order of 20 μm by about 10 μm in size. The plasma source ion column can deliver much higher beam currents to the sample at the expense of the size of the area of the beam. Thus, plasma sourced FIB columns are quite useful for preparing much larger samples (as large as 1 mm in width) than the LMIS FIB. The beam size of the plasma FIB is not as small as those that can be produced by LMIS sourced FIB tools. Selection of the plasma FIB over the LMIS sourced FIB depends on the end use. If larger cross sections of surfaces are to be routinely made then the plasma FIB may be the best choice. If TEM samples are more important, then the LMIS FIB may be the better choice. One also needs to keep in mind that the LMIS produces a beam of Ga+ ions that may react chemically with the sample. Plasma sources generally utilize inert gases (most commonly Xe) so chemical reactivity is not a concern. FIB instrumentation has been covered in detail elsewhere [11, 12].

To properly utilize any FIB tool, it is important for the user to have some understanding of the interactions that occur when an energetic ion interacts with the atoms in a sample. There are many events that occur when an energetic ion interacts with the atoms in a solid, but for the case of SEM and TEM sample preparation and ion imaging, we are mainly interested in sputtering (the removal of atoms from the surface of the sample), secondary electron production and damage to the sample in terms of ion implantation and loss of crystalline structure. Sputtering is the process that removes atoms from the target. Secondary electron production is important as images formed with secondary electrons induced by ions have some important advantages over secondary electron imaging. In principle, it is impossible to have an ion beam interact with a sample without causing some form of surface damage during ion irradiation.

Understanding the interaction of ions with the target material is helpful in reducing the amount of damage to acceptable or tolerable levels through appropriate sample preparation techniques. Energetic ions interact with a target in many ways. Once the ion enters the sample its path can be deflected by interactions with the atomic nuclei and the electron charges. As the ion moves through the sample it has sufficient energy to knock other atoms off their respective lattice positions. The target atoms that are knocked off their atomic positions can have enough energy to knock other target atoms off their atomic positions. This series of moving atoms and ions within the sample is referred to as a collision cascade. Some of the atoms that have been knocked from their atomic positions may reoccupy a lattice position or may end up in interstitial sites. There can also be lattice sites that are not reoccupied by target atoms and these are vacancies. Both interstitials and vacancies are considered damage to the crystalline structure of the sample. Most of the time, the original beam ion will end up coming to rest within the sample. This is termed ion implantation. Ion implantation results in the detection of the ion beam species in the sample and thus it is desired to minimize this as much as possible. Many of the collision cascades will eventually reach the surface of the sample. When the ion leaves the sample, it may have sufficient energy to knock an atom from the surface into the vacuum. This process is called sputtering and results in a net loss of material from the sample, usually from areas very close to the beam impact point. At the same time when the ion is either entering or leaving the sample, secondary electrons are generated that are useful for producing images of the sample surface scanned by the ion beam. It is important to remember that scanning an energetic ion beam over the surface of the sample will always result in some damage to the sample. The details of this process have been covered in other texts [10, 12].

It is most common to use the FIB to remove material to produce site-specific specimens via sputtering, but ions also produce secondary electrons that can be collected and imaged just like secondary electrons in the SEM. Ions generate many more secondary electrons than do electrons, thus ion induced secondary electron imaging can provide quality low-noise images. In addition, ions tend to channel more strongly than electrons and thus can produce striking grain contrast images. It is important to remember that during ion imaging of a sample, the continuous process of ion damage is occurring that will eventually (given sufficient time and ion dose) alter the sample to the point that it may no longer represent the original material.

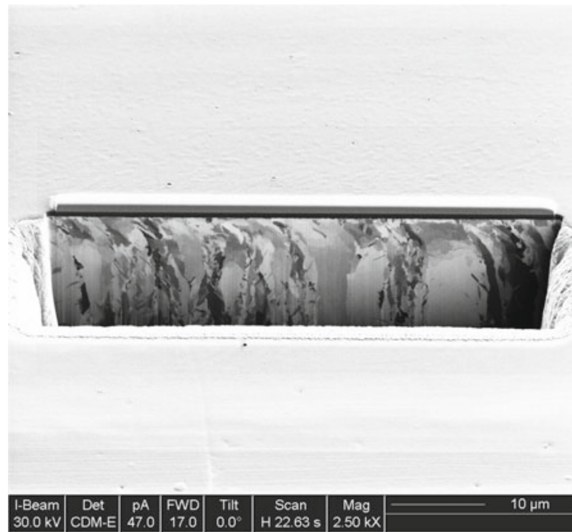

Fig. 1.2 Ion induced secondary electron image of a FIB prepared cross section of a wear scar (100 gm load for 1000 cycles) in Ni collected at 30 kV with an ion beam current of 47 pA. The dark layer on top of the Ni is a solid lubricant thin film

Figure 1.2 is a FIB prepared cross section of a wear scar produced by unidirectional sliding on electrodeposited Ni. This is an ion induced secondary electron (ISE) image obtained with a Ga+ ion beam using an accelerating voltage of 30 kV and a beam current of 47 pA. Note the high grain contrast produced by the ion beam and it is apparent that the stylus had moved from the right to the left-hand side of the image. The excellent grain contrast provided by ISE imaging provides useful insights into the wear process.

One common application of FIB is the preparation of cross sections of specific features. An example, as shown in Fig. 1.2, is that of a cross section normal to a wear surface that exposes sub-surface microstructural details. Cross sections prepared by FIB can vary from a few 10's of μm wide by a maximum of about 10 μm deep due to the time required to prepare the cross section. However, new developments in the use of plasma ion sources that can deliver much higher beam currents and thus faster milling rates have allowed sections to be milled as large as 1 mm wide by 10's of μm deep.

This text is not intended to describe in detail all of the steps required to produce quality cross sections as there are many texts already available that do this [11–13]. Cross sections of surfaces are accomplished in the FIB by careful control of the ion beam current. The first step of the process is to deposit a protective layer over the area of interest using electron or ion assisted deposition. Electron or ion assisted deposition is a process where a precursor gas is injected into the FIB through a needle that is very close to the sample surface. The electrons or ions in the beam disassociate the precursor resulting in a very impure Pt layer or a C layer to be formed only where the ion or electron beams are scanned during gas injections. The purpose of this protective layer is to prevent the energetic ions from interacting with the area of interest on the sample and causing damage as discussed previously. Once the

protective layer is applied, the ion beam is then used to remove material to expose a cross section of the area of interest. As the process continues lower ion beam currents are used to allow more precise ion milling of the area and to produce very smooth surfaces that are representative of the actual sample.

Another common application of FIB is the production of thin samples from specific sites that are suitable for transmission experiments in the transmission electron microscope (TEM) or in the SEM (scanning transmission electron microscopy in the SEM also called STEM in SEM or just STEM.). One other application that requires thin samples is transmission Kikuchi diffraction (TKD) [14, 15]. This technique is done in the SEM and provides high resolution (2–10 nm) orientation mapping of thin samples. No matter which application STEM or TKD is to be used, sample preparation requirements are very similar. First, the sample must be free (or as close as possible) of artifacts induced by the FIB milling process. Second, the samples must be very thin, usually less than 100 nm in thickness to allow the electrons to penetrate the sample. Modern FIB milling techniques have been developed that reduce or eliminate artifacts and allow extremely thin samples to be prepared and mounted so that the sample can be introduced into the STEM or SEM for imaging. This text is not intended to discuss all the methods of sample preparation as there are many complete texts on this subject [11, 12]. A brief discussion of the steps to produce thin samples with the FIB will be given.

Just as with cross sections made for SEM imaging the first step is to locate the area of interest and then protect this area with a layer of Pt or C deposited by either ion beam assisted or electron beam assisted deposition. Once this is done then trenches are placed on either side of the area of interest as the final thin sample will come from the material left in between these trenches. The sample thickness is carefully reduced by using decreasing beam current ion beams in the FIB until the desired thickness has been reached. At some point during the process (usually before the sample is at the final thickness) the ion beam is used to cut the sample free from the surrounding material so that it can be lifted out from the trench and placed on a suitable support for subsequent imaging. It is often advantageous to use a lower energy ion beam as a final step to remove the ion beam damage caused during the sample milling at higher energies. This step is extremely important when high resolution imaging in the TEM or STEM is to be done. Figure 1.3 is an example of a completed thin sample prepared by FIB milling. Here the sample has been thinned to the final dimensions and is ready to be manipulated to a suitable support for imaging. The sample is manipulated outside the FIB tool to the support and this is called ex situ lift-out [16]. Figure 1.4 shows the completed TEM specimen after manipulation to a carbon-coated TEM grid.

Thin samples may also be produced by in situ lift-out in the FIB system using an internal manipulator [17]. The general procedure adds a couple of steps to those described above. The first step is to excise a chunk of material from the bulk sample using the ion beam and the in situ manipulator. The chunk of material is then attached to a suitable grid or support structure and held in place with ion beam assisted deposition of Pt. The sample is then thinned by the removal of material from both sides of the sample until the desired thickness is reached. The advantage to in situ

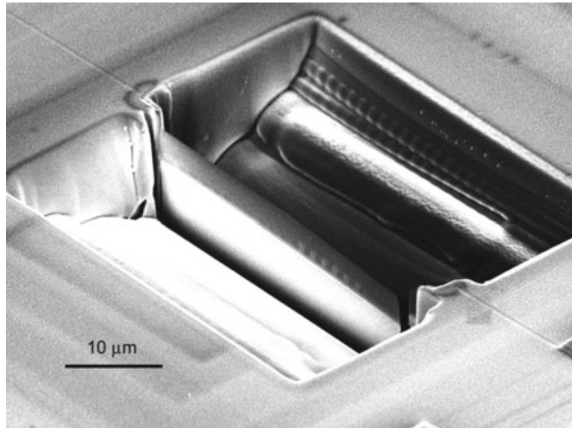

Fig. 1.3 Thin sample prepared by FIB that is ready for manipulation onto a suitable support for transmission imaging

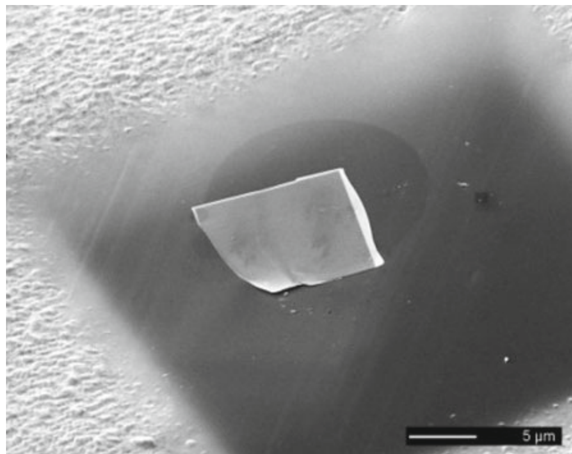

Fig. 1.4 FIB prepared thin sample manipulated onto a thin carbon film support

lift-out samples is that there is no support film to interfere with subsequent analysis and the sample is now firmly attached to the support structure and may be handled more easily.

The study of the evolution of sub-surface microstructures during wear requires that site-specific samples be produced. FIB tools can provide site-specific samples that are suitable for SEM imaging and analysis, TEM and STEM analysis. Many different types of samples can be produced in this manner that enhance the study of wear.

1.2.2 Electron Backscatter Diffraction and Transmission Kikuchi Diffraction

An understanding of the microstructure and crystallography of wear scars is required to fully describe the structure property relationships that control the tribological response of crystalline materials. By linking the microstructure to the crystallography of the sample, a full picture of the sample can be developed. Electron backscattering diffraction (EBSD) and the related technique of transmission Kikuchi diffraction (TKD) provide new insights into the microstructural changes that occur beneath a wear scar.

EBSD is accomplished in the SEM by the addition of a suitable camera to image the diffraction patterns and software to analyze the patterns and determine the crystallographic orientation of the sample. Most often, EBSD is conducted on polished bulk samples or bulk samples prepared in the FIB tool. Improved resolution over EBSD of bulk samples has been achieved by utilizing thin samples and TKD. TKD allows many of the fine details in wear microstructures to be observed. Both EBSD and TKD will be introduced in this section, and the reader is directed to many of the excellent texts available for more details [12, 18, 19].

EBSD patterns are obtained by illuminating a tilted sample surface with a stationary electron beam. The beam electrons interact with the sample and are initially inelastically scattered. The scattered electrons are diffracted by the crystalline planes in the sample to form the EBSD pattern that is then observed using a suitable camera. In the case of TKD, the thin sample is held normal or near-normal to the electron beam and the electrons transmit through the sample and are diffracted to form the TKD pattern. Note that EBSD and TKD patterns appear visually to be quite similar and can be indexed in the same manner (Fig. 1.5).

The EBSD pattern consists of sets of parallel lines. These are Kikuchi bands and the distance between the parallel pairs of lines is inversely related to the lattice spacing of the specific direction and the angles between the parallel sets of lines are the angles between the reflecting planes in the crystal. Thus, the angles between the planes can be compared to a table of angles prepared from known crystal structure data to determine the orientation of the patterns obtained from each pixel in an image.

EBSD or TKD orientation imaging is conducted by arranging the EBSD or TKD camera and the sample geometry in the SEM. The sample must be prepared so that the surface is free of preparation induced artifacts. Typically with bulk samples metallographic sample preparation is adequate and for TKD either FIB prepared surfaces or electropolished surfaces must be used. Figure 1.6 shows the arrangement of the sample and the EBSD or TKD cameras in the SEM. Note that a standard EBSD camera may also be used for TKD. The electron beam is scanned pixel-by-pixel over the areas of interest and patterns are collected at each pixel. The patterns are indexed and the orientation of the crystal is determined for each pixel. This procedure is repeated at each pixel within the image. Modern EBSD systems can now do this reliably at over 3000 patterns/sec allowing large areas to be efficiently imaged. Figure 1.7 shows inverse pole figure maps (IPF) of a wear scar made with a 10 g load

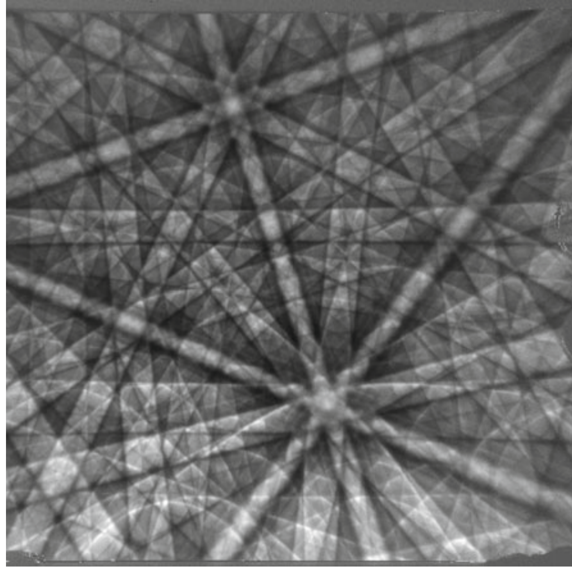

Fig. 1.5 EBSD pattern obtained from Mo at 20 kV

on a <111> single crystal of Ni. The wear scar was made in the <211> direction. The sample for these maps was made by FIB prepared thick lift-outs from the center of the wear scar. Figure 1.7a is the IPF map with respect to the surface normal and this is the <111> direction as can be seen by comparing the color of the substrate (blue) with the color key shown in Fig. 1.7c where the <111> directions on the stereogram is colored blue. Figure 1.7b is colored with respect to the wear direction and one can see that the <211> direction on the stereogram is between the blue of the <111> and the red color of the <100>. Thus by inspection it is relatively easy to understand the sample crystallography. In these images it is also apparent that the surface of the sample has been transformed from a single crystal to a layer of finer grained Ni with more random orientations.

An example of TKD of a wear scar in Ta is shown in Fig. 1.8. In this case a Co pin was worn against a Ta counterface. Note that this was obtained from a thin sample that was prepared for STEM imaging. The TKD maps were obtained using a 30 kV electron beam energy and a step size of 10 nm. Figure 1.8a is formed by a measure of the pattern's sharpness at each pixel and then plotting this as a grey scale image. The result accurately represents the microstructure of the sample. Figure 1.8b is an orientation map with respect to the wear direction (horizontal). Note that the upper part of Fig. 1.8b represents very fine grained wear debris that contains some very small grains that are just resolved.

EBSD and TKD are important characterization tools for wear phenomena in crystalline materials. TKD has the advantage of higher resolution while standard EBSD can provide data over larger areas at a reduced resolution.

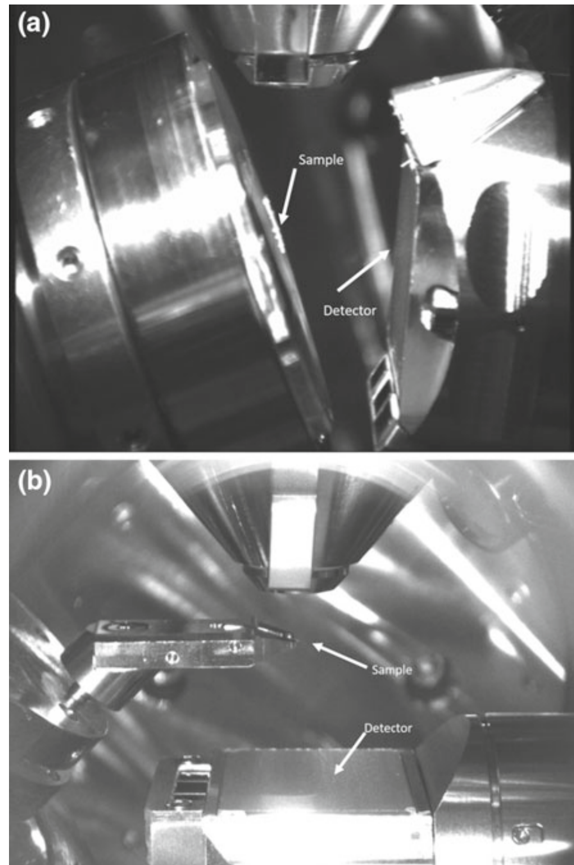

Fig. 1.6 Arrangement of the sample and the EBSD or TKD detectors in the SEM. **a** EBSD **b** TKD

1.3 Transmission Electron Microscopy and Microanalysis

Transmission electron microscopy (TEM) encompasses a few powerful techniques for characterizing wear surfaces at length scales from 100 pm to tens of μm. Since electrons interact strongly with matter we need to use high-energy electrons (100–300 kV) and create thin specimens (~100 nm in transmission). Before the advent of the FIB, the challenge was making a sample in the desired location and an appropriate thickness in projection. As discussed above the FIB now allows for routine creation of site-specific TEM samples which in many cases would be difficult or impossible to do by many using conventional sample preparation methods. In this section we will discuss the basic imaging methods of TEM, diffraction, and microanalysis and related data analysis methods.

In this section we give a general overview of TEM and associated techniques. The reader is directed to the text by Williams and Carter [7] for more detail on TEM and to Carter and Williams [20] for advanced discussion of TEM techniques including this

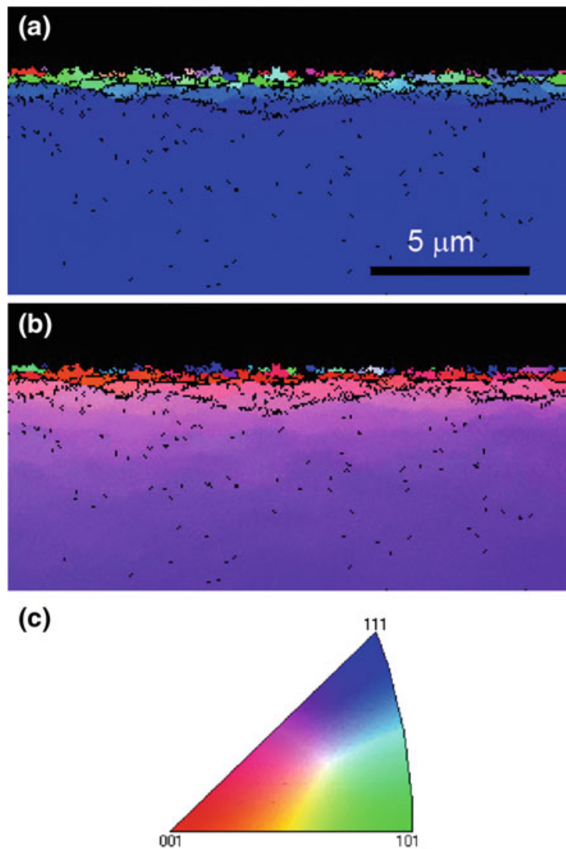

Fig. 1.7 Inverse pole figure maps obtained from wear scars on <111> single crystal Ni substrates. **a** IPF with respect to sample normal, **b** IPF with respect to wear direction, **c** color key for IPF maps

section's discussion of microanalysis (spectral imaging and data analysis methods). The TEM is analogous to a light microscope. We have an electron instead of light source, electromagnetic instead of glass lenses, condenser lenses which structure the electron illumination on the specimen, an objective lens, projection lenses and detectors to record the images. Since electrons interact strongly with matter we need to use both high-energy electrons, typically 100–300 kV, and thin specimens typically 100 nm thick or less in the projection direction. As with light microscopes we can think of the resolving power in terms of the wavelength of the illuminating light or in the case of TEMs the electrons which are 3.7 pm at 100 kV and 2 pm at 300 kV (at these energies the electrons are relativistic). One of these requirements, electron energy, leads to additional characterization capabilities to TEMs allowing us to analyze crystallography of our materials. In particular, the wavelength of the electrons (which are relativistic and thus act as both particles and waves) is smaller than the crystallographic plane spacings in materials which are typically 1 nm and

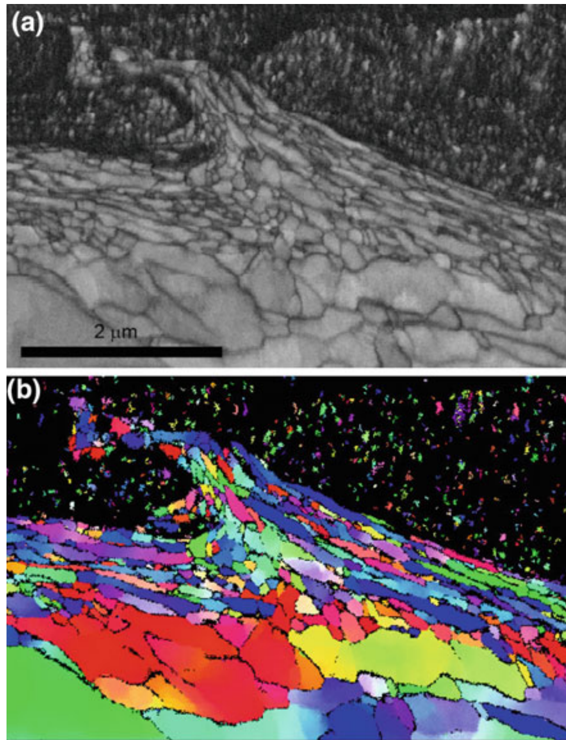

Fig. 1.8 TKD of Ta worn with a Co pin collected with a 10 nm step size. **a** A band contrast image formed by a measure of the collected patterns sharpness at each point in the image. **b** Orientation map with respect to the wear direction. Note that the colors represent orientations as shown in Fig. 1.7c

smaller, so that we get diffraction. Additionally, given the samples must be thin and analyzed in transmission we can improve the resolution of microanalysis versus a SEM. This will be discussed in the following sections.

1.3.1 Transmission Electron Microscopy

TEM is both a general term describing an instrument and technique, namely passing electrons through a specimen, and a specific term referring to the use of broad electron illumination on a specimen. In this sense, it is analogous to the basic visible-light microscope. However, because electrons interact strongly with matter, the electrons can be scattered or diffracted multiple times while passing through a specimen. This can be used to great advantage for imaging defects like dislocations and stacking faults. Additionally, twins, precipitates, cracks, and amorphous regions can be imaged

in the conventional TEM modes. The types of data typically acquired for this include bright-field (BF) and dark-field (DF) images which are distinguished by the use of a small objective aperture (placed in the back-focal plane of the objective lens where a diffraction pattern is located) centered on the direct or a diffracted beam respectively. In TEM (specific definition) we have broad illumination on the sample (created by the condenser lenses). The sample sits within the objective lens which has two parts, an upper lens and a lower lens. The upper objective lens is used for focusing the illumination to a point, and this is important for scanning-TEM (STEM). The lower objective lens is the image-forming lens. Depending on how the projector lenses are set we can form an image of our specimen, or a diffraction pattern on the detectors. The former setting is used to collect a BF, DF or other image. The latter setting allows us to collect a diffraction pattern. Furthermore, we can place an aperture at a conjugate image plane within the projector lens system. This aperture can be moved to capture a small image region from the specimen. By then switching to diffraction mode, we can see a selected-area diffraction (SAD) pattern. BF, DF and SAD are powerful methods for characterizing and surveying the coarse-scale structure of a specimen.

In order to take advantage of the resolving power of the TEM we must operate in a different mode, high-resolution TEM (HR-TEM). In this operational mode, we use a larger objective aperture which allows the phase of several diffracted beams to interfere. In this way can resolve lattice planes from a specimen provided they are oriented parallel to the electron beam and of a sufficient spacing to be resolved by the microscope. Recent advances in electron optics, namely the commercial availability of spherical aberration correctors, have allowed for routine resolution of sub-100 pm lattice spacings [21]. HR-TEM is useful for imaging basal planes in graphite and MoS_2 especially when aligned parallel to the electron beam as in looking at the cross-section of a wear surface with those solid lubricants.

1.3.2 Scanning Transmission Electron Microscopy

STEM is analogous to SEM in that we focus the electrons to a point on the specimen and then scan it across our specimen. We then get contrast from the specimen with one of several possible detectors. These detectors sit below the projector lenses at a conjugate diffraction plane and the projector optics can be changed to magnify or de-magnify the diffraction pattern on the various detectors. By reciprocity [7] we can form images equivalent to conventional TEM BF and DF images in STEM mode. We can also form images with electrons scattered out to higher angles. These are called high-angle annular dark-field (HAADF) images and contrast from the specimen (presuming constant sample thickness in projection) is proportional to average atomic number. STEM is a versatile imaging mode for looking at both coarse structure (tens of microns) and atomic or near-atomic resolution 0.3 nm (lattice in some materials is resolvable) in a conventional STEM. As with TEM, spherical aberration correctors [22] have been developed for STEMs and have pushed direct resolution to 0.08 nm

or better. It's important to provide a caveat for such resolution numbers, namely that these numbers are for a crystalline specimen oriented with lattice planes parallel to the electron beam and are dependent on electron channeling. For a specimen that is amorphous or not in a special orientation, the beam will broaden as it passes through lowering the actual resolving power.

1.3.3 Microanalysis

When a high-energy electron hits a specimen, it's possible for electrons to be knocked out of atoms in the specimen. As a result of the subsequent electronic relaxation, one possibility is that X-rays will be emitted from the excited atoms. The energy of the emitted X-rays is characteristic of the elements present in the specimen. Therefore we can use our electron probe to perform X-ray microanalysis to understand the local chemistry of our specimen with sensitivity (varies by element) to the entire periodic table above Li. As with SEMs, we can add an X-ray detector to detect the X-rays emitted from the specimen. In the SEM, the resolution of this signal is complicated and dependent upon both the elements in the specimen and the energy of the incident electrons. The volume from which X-rays are emitted is known as the interaction volume. In some cases, this can be a micron or more. This provides a distinct advantage in resolution for TEM specimens where the bulk of material has been removed, leaving only a thin lamella of material from which X-rays can be generated and subsequently detected. The result of this is that fewer X-rays are generated compared with a typical SEM specimen. The benefit is that the X-rays that are generated come from a region comparable to the electron probe plus the amount that the beam broadens as it passes through the specimen. The electron beam will broaden more in a high atomic number material than in a lower one of similar thickness. Thinning the specimen can improve resolution but at the expense of less material which can generate an X-ray signal. Modern analytical electron microscopes (AEM) are STEMs with X-ray and other chemically sensitive detectors (e.g., electron energy-loss spectrometers). To make up for the smaller number of X-rays generated by thin samples, X-ray detectors with larger solid-angles of collection have been developed so that 0.5 steradians to 1 steradian systems are commercially available [23]. For comparison, older AEMs typically had solid-angles of collection of 0.06 steradians.

There are a number of ways we can interrogate our specimen with X-ray microanalysis. The simplest is to manually move the electron beam to a feature and collect a single high-signal spectrum. This can be repeated on additional features but entails a significant amount of subjectivity with respect to appropriate sampling. Did we sample enough regions? And what if regions with important chemical differences show the same image contrast? Will we sample those? X-ray microanalysis has undergone a number of advances in the past 25 or so years. The most important was the advent of spectral imaging systems for commercial X-ray detectors on SEMs [24] and later STEMs. A spectral image combines imaging with full spectrum acquisition. A spec-

tral image consists of a full X-ray spectrum at each pixel in an image. We then are statistically sampling many different points in a regular array. The next most important development was the development of the silicon-drift detector (SDD) [25]. In its modern form [26, 27] the SDD has completely replaced the older liquid nitrogen cooled Si–Li technology [28]. SDDs are cooled to −20 °C allowing for windowless operation improving light-element sensitivity. They are also able to operate at higher X-ray fluxes (over 1 MHz is possible but practical only for an SEM geometry) at near theoretical resolution. Since the cooling requirements are less stringent compared with older detectors, novel geometries have been implemented [29, 30] improving solid-angle of collection in the AEM by more than ten times [23].

Spectral imaging solved the problem of sampling but created a new one, namely how to analyze all the data comprehensively. In the next section, we discuss conventional and advanced data analysis methods.

1.3.4 Spectral Image Analysis

In order to understand the structure and chemistry of our specimen with an AEM, we collect electron images and spectral images. We can make direct measurements from the images (e.g., film thickness, crack length, phase fraction, etc.) but the spectral images are more complex, consisting of tens of thousands to hundreds of thousands of spectra (pixels) each with 2000 energy channels typically. The challenge is how to comprehensively analyze the sheer quantity of data we can quickly generate on a modern AEM. The spectral image lends itself to retrospective analysis in that we can collect the data on the AEM and then analyze and re-analyze it offline.

Conventional analysis of a spectral image is an iterative process [20, 31] starting with looking at the sum of all the spectra in the spectral image. We can then form region-of-interest maps of the elements identified from that spectrum. From the maps, we can identify regions in the image and look at sum spectra from identified regions. This forms the basis to confirm the analytical results. In X-ray spectroscopy, there are a number of artifacts in maps. These include Bremsstrahlung or breaking radiation generated as electrons in the specimen are decelerated. The result is a continuum X-ray background which is stronger for heavy elements than for light elements. Looking only at a map for a light element like oxygen, in a specimen with a heavy element like gold will illustrate the artifact. Regions with gold will produce a large background signal. In the oxygen map, regions with gold but not oxygen will show elevated intensity. This can be visualized by looking at spectra from the gold regions and verifying that no oxygen is present. More importantly we can see that oxygen is present by looking at spectra from the other distinct regions in the oxygen map to verify the presence of oxygen. An additional artifact in X-ray spectroscopy comes from the fact that different elements and have X-ray lines at the same energy. For example, the silicon K line is at 1.739 kV while the tantalum M-α line is at 1.709 kV. The result is that the silicon map will show intensity everywhere there is Ta. Also, depending on which tantalum line we use to form the Ta map we might see

silicon where it is not. Using the iterative analysis approach, we can help solve such pathological overlap problem cases.

Conventional analysis can be time consuming and subjective. We can also miss important features due to the artifacts mentioned above as well as just miss a weak but potentially important feature. For these reasons, we discuss the use of statistical analysis methods to quickly and comprehensively analyze X-ray spectral images with no preconceptions of what is or is not present.

1.3.5 Multivariate Statistical Analysis

Multivariate statistical analysis (MSA) encompasses a family of data analysis methods that are used to visualized data sets subject to various constraints. For X-ray spectral images the number of variables is typically the number of spectral channels, perhaps 1000–2000. Understanding how collections of these co-vary can be used to understand the chemistry of a specimen. One can think of the channels containing a particular spectral peak or families of peaks as co-varying when the element responsible for the peaks is present in regions in the specimen. Similarly, elements found together in the same amounts in regions of the specimen would produce channels that co-vary.

Before we discuss different MSA methods, it's important to discuss scaling the raw X-ray spectral image data for non-uniform noise [32, 33] and estimating the rank of the data. When we discuss X-ray spectroscopy we have X-ray counts where the noise is proportional to the signal. If we fail to account for the noise in our MSA methods then we risk fitting noise when it is greater in magnitude than weaker but chemically relevant signals in the spectral image. If we have a channel in our data where the intensity is 100 counts, the associated noise for that datum is the square root of 100 or ± 10. Variance-based MSA methods would preferentially fit such a variation over a chemical signal smaller than that. Noise scaling, for the purpose of the examples described in this chapter, amounts to dividing the spectral image by the square root of the mean spectrum in the spectral domain and the square root of the mean image in the image domain [32, 33]. Once we have performed the noise normalization, we can then calculate the eigenvalues from the scaled spectral image data. The sorted eigenvalues on a semi-log plot are referred to as a scree plot, an example of which is given in Fig. 1.9. Here we examine just the 64 largest eigenvalues. Sandia's Automated eXpert Spectral Image Analysis (AXSIA) software [34–36] performs an automated rank estimation by fitting a straight line to eigenvalues indexed 25 through 64, a region assumed to represent the noise baseline. When an eigenvalue rises above the fit to the line by greater than 25 σ it is deemed non-noise and usually represents chemical information. The index of this eigenvalue is the estimated rank, or number of components needed to describe the data minus the noise.

Following noise normalization and rank estimation we then factor the data into a form we can readily interpret. The reader may be familiar with one MSA variant called Principal Components Analysis (PCA) [37]. PCA seeks to serially maximize the

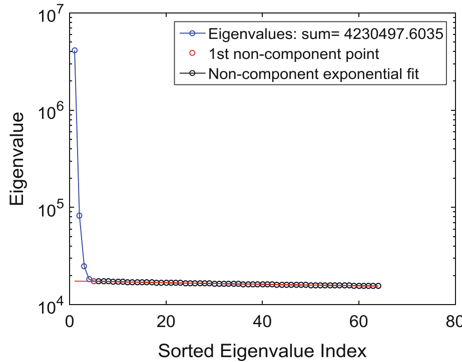

Fig. 1.9 Scree plot showing the results of an Eigenanalysis of a spectral image weighted for non-uniform noise. The automatically determined rank for the model of the data is four meaning that only four factors are needed to describe the chemical information in the spectral image consisting of hundreds of thousands of pixels and thousands of spectral channels

variance in components which are mutually orthogonal. The first principal component is the mean. The second principal component describes the second most variance in the data while being orthogonal to the first and so on. The problem with PCA is that the constraints (serial maximization of variance and orthogonality) result in non-physical components consisting of a component image and corresponding spectral shape which both consist of positive and negative intensities. For this reason we add an additional assumption to the factor analysis that none of the component images or spectral shapes has negative (non-physical) intensities. The non-negativity constraint relaxes the orthogonality imposed by PCA such that the resulting factors now are directly interpretable. AXSIA achieves this via application of a MSA technique called multivariate curve resolution (MCR) implemented by an alternating least squares (ALS) approach [36]. The rotational ambiguity, the fact that there are an infinite number of solutions to fit the data equally well, is addressed by performing a Varimax rotation [38] on the data to make it simple in either the spectral [34–36] or spatial [39] domain. Simple implies high contrast or zeros in many parts of the components. The end result for both spectral and spatially simple representations is a compact and physically interpretable model for the data. The factors making up this model contain spatial components and corresponding spectral shapes. The component images tell us where and how much of the elements are present, and the spectral shapes tell us the identities of the elements.

1.4 Tribology Case Studies

This section describes a few specific examples on the application of these novel electron microscopy techniques in tribology and tribological coatings.

1.4.1 Diamond-Like Carbon Coating Characterization

The most widespread application of FIB in tribology is in the characterization of the coatings on miniature parts, specifically those on the sidewalls of microelectromechanical systems (MEMS). With miniaturization, the surface interactions play a predominant role in determining the performance and reliability, necessitating the need for solid lubricating coatings. Most of the commercial coatings are deposited by physical vapor deposition processes, which are inherently line-of-sight. FIB has become an invaluable tool in the characterization of thin films and coatings on the sidewalls of miniature parts and on buried interfaces. The example shown in Fig. 1.10 is from our earlier study on the application on diamond-like carbon on Ni Microsystems part fabricated by LIGA (German acronym for lithography, electroforming, and molding). The DLC coating was applied by a commercial plasma enhanced chemical vapor deposition technique. TEM analysis was used to assure that the DLC coating coverage on the sidewalls, where it is most needed, is dense, conformal and without any interfacial defects [40].

1.4.2 Wear-Induced Recrystallization

The first reported application of EBSD for the study of wear-induced recrystallization in metals was on electroplated Ni surfaces [41]. Figure 1.11a shows the location of the FIB cut on the wear surface created by a Si3N4 ball at an initial Hertzian contact stress of 315 MPa for 1000 cycles of sliding in unidirectional mode. The direction of sliding was from left to right, as shown by the arrow. The electroplated Ni had a predominantly <001> fiber texture. There also appears to be a fine-grained region near the top, i.e. right underneath the wear track. Figure 1.11b is the orientation map of the substructure underneath the wear track. The colors represent the orientations normal to the sample surface based on the color key shown in the inset. This is an interesting area as there is a region that has a <110> fiber texture (designated by green) in the predominantly <001> fiber textured material. The thick and thin black lines represent high- and low-angle grain boundaries respectively. Figure 1.11b clearly reveals two characteristic zones, each with its own unique features which differ significantly from the microstructure in the bulk undisturbed material. A few microns below the wear track, the bending of columnar grains in the direction of sliding is observed, which is referred to as “Zone 1”. As we approach the wear surface, a lineup of thin black lines appears in the microstructure indicating the formation of substructures within the deformed zone. Right underneath the wear track, the columnar structure broke down into more equiaxed submicron-size grain structure, which is referred to as “Zone 2”. The depth of this zone extends to 1–2 μm. Zone 1 and Zone 2 are also referred to as “plastically deformed” and “highly deformed” zones respectively. It is also interesting to note that Zone 2 is thicker in the <110> fiber textured region than in the <001> fiber textured region. The pole figures corresponding to <001>

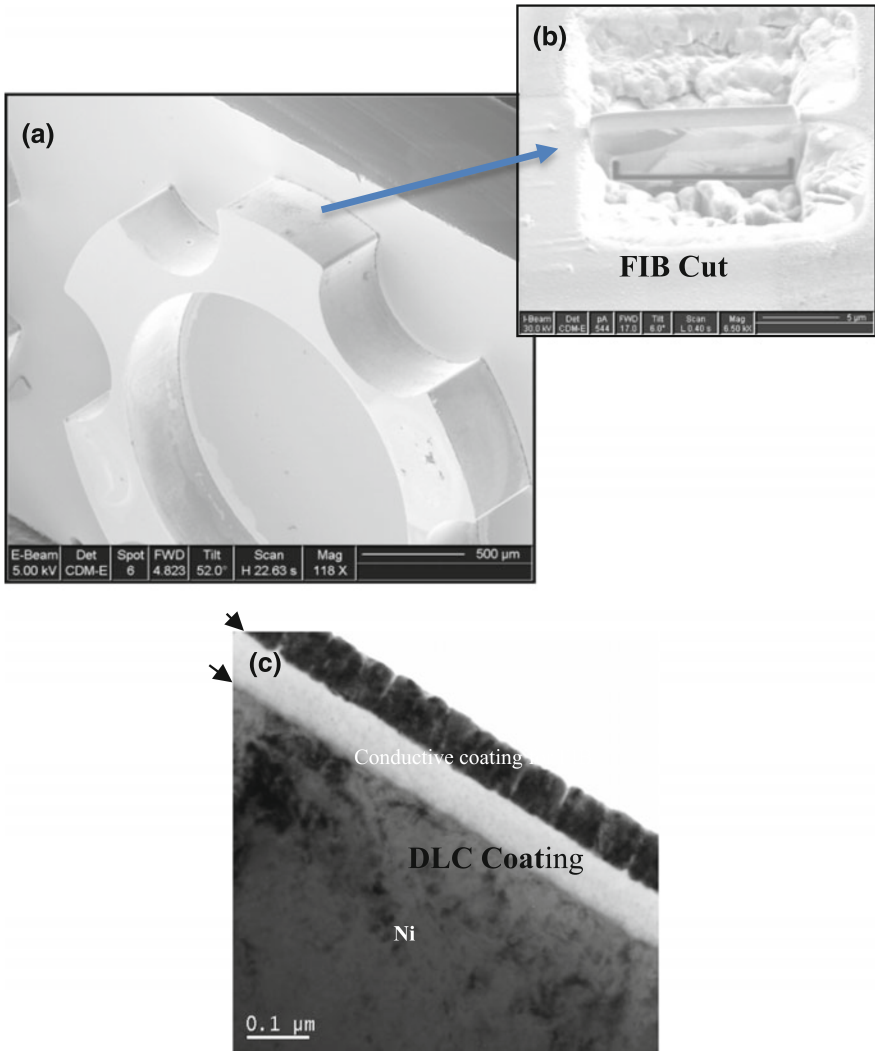

Fig. 1.10 **a** SEM micrograph of a Diamond-like carbon coated Ni-based microsystems part fabricated by LIGA, **b** FIB cut on the sidewall to prepare a TEM sample, **c** Bright-filed TEM image of the FIB cut showing the DLC coating on the sidewall. Reproduced by permission of IEEE Xplore [41, Figs. 3 and 8]

and <110> textured grains are shown in Fig. 1.11c. The spread in orientation of pole figures (Fig. 1.11c) can be used to judge the extent of wear-induced deformation in the subsurfaces. The <110> textured grains have wider orientation spread in the sliding direction (18°–44°) than the <001> textured grains (10°–17°), which is in agreement with the microstructural findings in Fig. 1.11b.

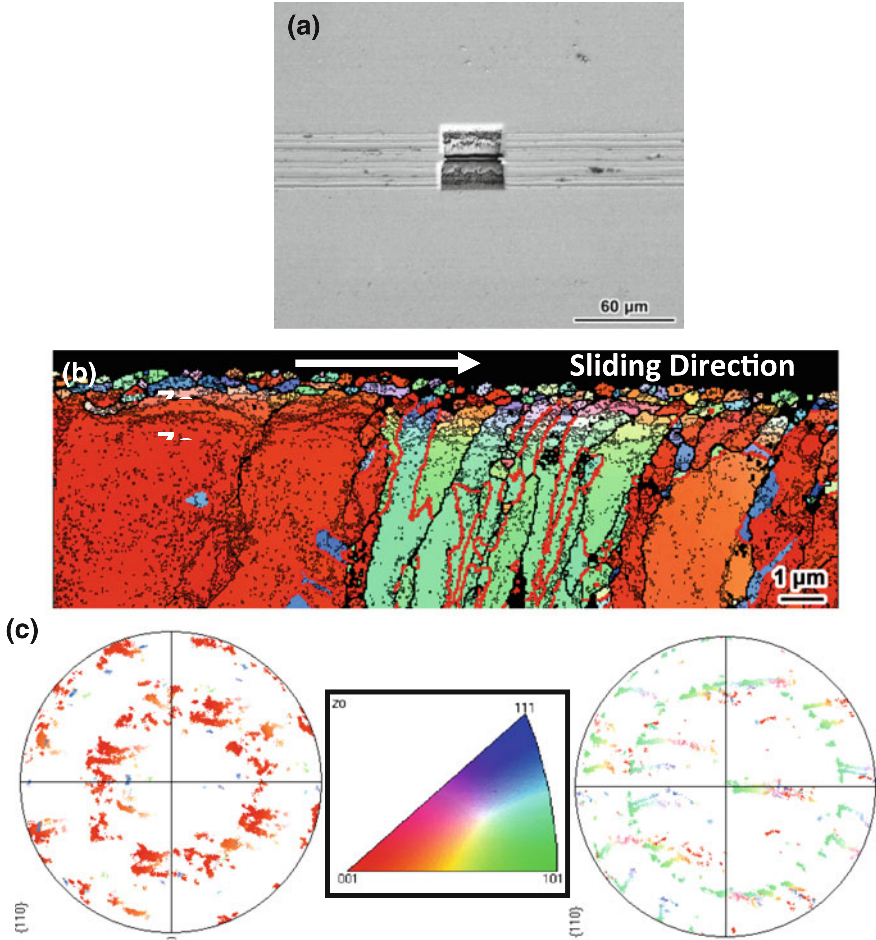

Fig. 1.11 EBSD analysis on the subsurface of a wear scar on electroplated Ni. **a** Location of the FIB cut on the wear scar; **b** orientation map with respect to the surface normal (the arrow represents the sliding direction); the heavy black lines represent orientation changes >10° and thin lines represent orientation changes of 1° or less, **c** pole figures of the region underneath the wear scar showing <001> and <110> fiber textured material (sliding direction is Y0). Inset at the center of Figure **c** is the stereographic triangle with color key for (**b**). Reproduced by permission of Pergamon Press [40, Fig. 3]

This very first study on the application of EBSD for friction-induced wear phenomena has demonstrated the unique role of focused ion beam techniques in preparing cross sections of narrow wear tracks generated under very light loads for electron backscatter diffraction studies. By suitably thinning the samples further, this technique can be easily extended to prepare cross sections of wear tracks for TEM

analysis. Unlike in conventional specimen preparation techniques, the FIB enabled specimens are free of artifacts introduced during dicing, grinding, electropolishing, dimpling, etc., and sections can be precisely cut at a specific location on the wear track.

1.4.3 Tribology of Nanocrystalline Metals

While the deformation behavior in metals with relatively large grain sizes is predominantly dictated by dislocation dynamics, gain boundary processes dominate in the nanocrystalline regimes, when the grain sizes are below 20 nm [42]. Analogous to the grain size dependency on the mechanical behavior, recent studies seem to confirm that friction behavior of nanocrystalline metals could be significantly altered when the friction-induced deformation results in the formation of stable ultrananocrystalline structures in the subsurfaces. This was first highlighted by Prasad, Battaile and Kotula [42] from their study on friction behavior of nanocrstalline nickel, which exhibited two distinct friction behaviors, $\mu \sim 0.30$–0.35 or $\mu \sim 0.6$–0.7, depending upon the contact stress and sliding speed (Fig. 1.12a).

Figure 1.12b is an annular dark field STEM image showing detailed features of the subsurface for the case which exhibited low friction behavior (green circles in Fig. 1.12a). The arrow indicates the direction of sliding. The image shows three zones (labeled in Fig. 1.12b). The zones observed include an ultrafine grained region directly at the wear surface (Zone 1), a region with large, textured, flattened grains (Zone 2), and a gradual transition of grain size approaching that of the bulk material (Zone 3). The bulk has an average grain size of 20–100 nm. During frictional contact at stresses and sliding speeds corresponding to the green circles in Fig. 1.12a, ultrafine nanocrystalline gains with a size of 2–10 nm formed right underneath the wear surface (Zone 1). The authors attributed the experimentally observed transition from high friction to low friction regime to the formation of this ultrafine nanocrystlline structure underneath the wear surface elucidated by FIB-TEM. The authors also reported that in Zone 1 microstructure was absent in cases that did not exhibit a friction transition. Zone 2 consisted of platelet shaped grains larger than 100 nm, elongated in the sliding direction, in between Zone 1 and the bulk microstructure of Zone 3. The grains in Zone 2 represent a layer approximately 150 nm thick that showed significant grain growth and the development of crystallographic texture. Additionally, the transition between Zones 2 and 3 is not sharp but rather graded as the grain size returns to bulk dimensions over a distance of a few hundred nanometers. The study is a clear demonstration of the application of modern electron microscopy techniques for the fundamental understanding of the mechanisms of friction in nanocrystalline metals.

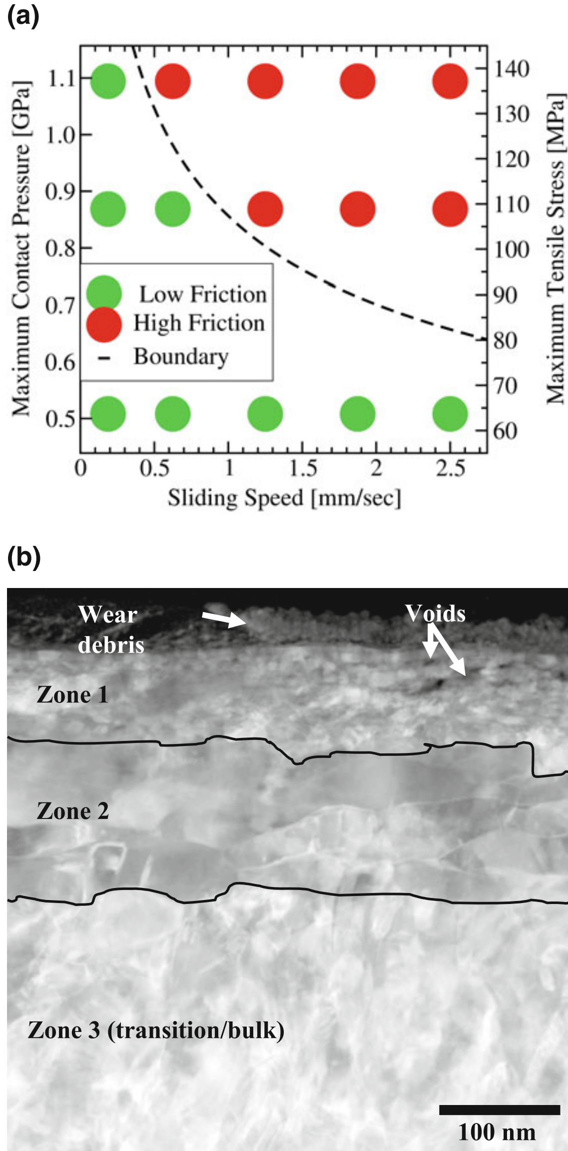

Fig. 1.12 **a** Friction transitions in nanocrystalline Ni [42]. The data was generated over a wide range of contact pressures and sliding speeds. The green dots represent the low friction regime while the red dots correspond to the high friction regime. The dotted line depicts the friction transition. **b** Annular dark field STEM image of the subsurface frim the low friction regime, showing ultrananocrystlline grain structure at the top. Reproduced by permission of Pergamon Press [42, Figs. 2 and 3b]

1.4.4 Transition Metal Dichalcogenides

Transition Metal Dichalcogenides (TMD), most notably, molybdenum disulfide (MoS_2) and tungsten disulfide (WS_2) are well known for their solid lubricating behavior and are widely used in several applications. MoS_2 crystallizes in the hexagonal structure where a sheet of molybdenum atoms is sandwiched between two hexagonally packed sulfur layers with a high *c*/*a* ratio ($c = 12.29$ Å, $a = 3.16$ Å). The bonding within the S–Mo–S sandwich is covalent, while weak Van der Waals forces hold the sandwich together resulting in interlamellar mechanical weakness. It has been widely reported [43] that under a shearing force the basal planes slide over one another by intracrystalline slip, similar to a 'deck-of-cards', resulting in the formation of a transfer film on the rubbing counterface (e.g., the ball surface in a ball-on-disk friction and wear test), shown schematically in Fig. 1.1. According to the widely accepted hypotheses, the main mechanisms for imparting low interfacial shear in TMD are: creation of (0002) basal planes and subsequent (re)orientation parallel to the sliding direction, and the development of a transfer film on the counterface to accommodate interfacial sliding. Until the advent of FIB, preparing TEM samples of these thin layers transferred onto the ball surfaces from ball-on-disk tribology tests of MoS_2 films that are suitable for high resolution lattice imaging has not been very successful. A recent study by Scharf, Kotula and Prasad [43] demonstrated the application of FIB to prepare TEM samples of transfer films form a molybdenum disulfide film doped with antimony trioxide and gold (MoS_2–Sb_2O_3–Au). This film, which has been successfully deployed in several space mechanisms, lacks any long-range crystallinity in the as-deposited condition. Using FIB-TEM, these authors have reported the presence of a thin layer at the top of the cross-section of the wear surface that has crystalline 2H–MoS_2 basal (0002) planes aligned parallel to the sliding direction (Fig. 1.13b). The arrow indicates the sliding direction, while the region above the arrow corresponds to the carbon film that was applied as part of the TEM FIB sample preparation. Just below this crystalline 2H–MoS_2 layer, the TEM image in Fig. 1.13b shows the presence of ~4–6 nm Au particles that are larger than the 2–3 nm size nanoparticles in the as-deposited coating seen in the bulk. This Au nanoparticle coarsening is clearly a result of the sliding process. The AXSIA map in Fig. 1.13d (where red is MoS_2/Sb_2O_3/Au and green is Au) also confirms Au particle coarsening due to frictional contact. A typical HRTEM image of a FIB cross-section of the transfer film (Fig. 1.13a) showed that it was comprised of predominantly crystalline MoS_2 through its entire thickness of ~1 μm. However, in the top layer, the basal planes are aligned parallel to the sliding direction. This layer is about 6 nm thick, which approximates to nine basal planes of MoS_2. A SAD pattern obtained from this top most region of the cross-section (Fig. 1.13c) showed that the interlamellar

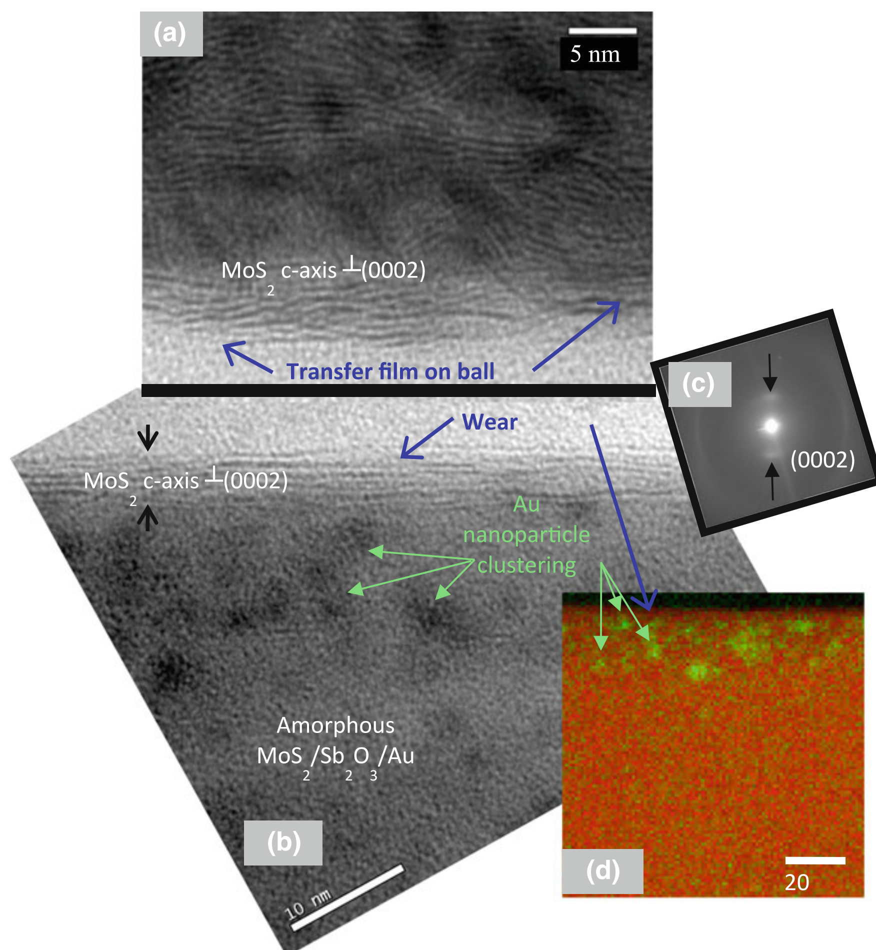

Fig. 1.13 **a** and **b** Cross-sectional HRTEM montage images of wear track on $MoS_2/Sb_2O_3/Au$ solid lubricant film with its transfer film on the ball surface. **c** SAED pattern of transfer film with interlamellar d-spacing between the (0002) $2H_2$–MoS_2 planes measured at ~6 Å, which compares well with indexed 6.1 Å lattice spacing of MoS2. **d** AXSIA results of the wear surface where red is $MoS_2/Sb_2O_3/Au$ and green is Au (with some Sb/O). Reproduced by permission of Pergamon press [43, Fig. 9]

d-spacing between the (0002) 2H–MoS_2 planes was ~6 Å, which compared well with indexed (PDF#01-087-2416) 6.1 Å lattice spacing for MoS_2 lattice. Once again, the application of modern electron microscopy and microanalysis techniques has been able to experimentally validate the widely held concept of self-mated 'basal plane-on-basal plane' sliding as the fundamental mechanism of lubrication in transition metal dichalcogenide thin films.

Acknowledgements Sandia National Laboratories is a multi-mission laboratory managed and operated by National Technology and Engineering Solutions of Sandia, LLC., a wholly owned subsidiary of Honeywell International, Inc., for the U.S. Department of Energy's National Nuclear Security Administration under contract DE-NA0003525. The authors gratefully acknowledge Professor Thomas W. Scharf, University of North Texas, for many years of collaboration with the authors on this subject, and Dr. Corbett Battaile for critically reviewing the manuscript. Special thanks to Michael Rye for the FIB work and to Bonnie McKenzie for the SEM, EBSD and TKD studies.

References

1. D.A. Rigney, J.P. Hirth, Plastic-deformation and sliding friction of metals. Wear **53**, 345–370 (1979)
2. S.V. Prasad, Wear, in *Concise Encyclopedia of Advanced Ceramic Materials*, ed. by R.J. Brook (Pergamon Press, Oxford, 1991), pp. 511–519
3. S.V. Prasad, T.W. Scharf, J. Mater. Sci. **48**, 511–531 (2013)
4. A.J.W. Moore, Proc. Roy. Soc. A **195**, 231 (1948)
5. F.P. Bowden, D. Tabor D, *The Friction and Lubrication of Solids* (Clarendon Press, Oxford, 1986), pp. 112, 120
6. R.F. Pease, W.C. Nixon, J. Sci. Instrum. **42**, 81–85 (1965)
7. D.B. Williams, C.B. Carter, *Transmission electron microscopy: A Textbook for Materials Science*, 2nd edn. (Springer, 2013) ISBN-13: 978–0387765006
8. P. Heilmann, D.A. Rigney, Metall. Trans. **12A**, 686 (1981)
9. W.M. Rainforth, Wear **245**, 162 (2000)
10. M. Nastasi, J. Mayer, J.K. Hirvonen, *Ion-Solid Interactions: Fundamentals and Applications* (Cambridge University Press, New York, 1996)
11. L. Giannuzzi, *Introduction to Focused Ion Beams: Instrumentation, Theory, Techniques and Practice* (Springer, New York, 2006)
12. J.I. Goldstein, D.E. Newbury, J.R. Michael, N.W.M. Ritchie, J.H. Scott, D.C. Joy, *Scanning Electron Microscopy and X-Ray Microanalysis* (Springer, New York, 2017)
13. J. Mayer, L.A. Giannuzzi, T. Kamino, J. Michael, TEM sample preparation and FIB-induced damage. MRS Bull. **32**(5), 400–407 (2007)
14. P.W. Trimby, Orientation mapping of nanostructured materials using transmission Kikuchi diffraction in the scanning electron microscope. Ultramicroscopy 16–24 (2012)
15. R.R. Keller, R.H. Geiss, Transmission EBSD from 10 nm domains in a scanning electron microscope. J. Microsc. 245–251 (2012)
16. L.A. Giannuzzi, Z. Yu, D. Yin, M.P. Harmer, Q. Xu, N.S. Smith, L. Chan, J. Hiller, D. Hess, T. Clark, Theory and new applications of ex situ lift out. Microsc. Microanal. **21**(4), 1034–1048 (2015)
17. N. Bassim, K. Scott, L.A. Giannuzzi, Recent advances in focused ion beam technology and applications. MRS Bull. **39**(4), 317–325 (2014)
18. V. Randle, *Microtexture Determination and its Applications* (Maney Publishing, London, 2003)
19. A.J. Schwartz, M. Kumar, B.L. Adams, D.P. Field (eds.), *Electron Backscatter Diffraction in Materials Science* (Springer, New York, 2009)
20. C.B. Carter, D.B. Williams (eds.), *Transmission Electron Microscopy* (Springer International Publishing Switzerland, 2016), Chapter 16, https://doi.org/10.1007/978-3-319-26651-0_16
21. M. Haider, S. Uhlemann, E. Schwan, H. Rose, B. Kabius, K. Urban, Electron microscopy image enhanced. Nature **392**, 768–769 (1998). https://doi.org/10.1038/33823
22. P.E. Batson, N. Dellby, O.L. Krivanek, Sub-ångstrom resolution using aberration corrected electron optics. Nature **418**, 617–620 (2002). https://doi.org/10.1038/nature00972

23. H.S. von Harrach, P. Dona, B. Freitag, H. Soltau, A. Niculae, M. Rohde, J. Phys.: Conf. Ser. **241**, 012015 (2010)
24. R.B. Mott, C.G. Waldman, R. Batcheler, J.J. Friel, Position tagged spectrometry: A new approach for EDS spectrum imaging. in *Proceeding of Microscopy Microanalysis*, ed. by G.W. Bailey, M.H. Ellisman, R.A. Hennigar, N.J. Zaluzec. Jones and Begell Publishing, New York, pp. 592–593
25. E. Gatti, P. Rehak, Nuc. Inst. Meth. Phys. Res. **225**, 608–614 (1984)
26. L. Strüder, N. Meidinger, D. Stotter, J. Kemmer, P. Lechner, P. Leutenegger, H. Soltau, F. Eggert, M. Rohde, T. Schulein, High-resolution X-ray spectroscopy at close to room temperature. Microsc. Microanal. **4**, 622–631 (1998)
27. A. Niculae, P. Lechner, H. Soltau, G. Lutz, L. Strüder, C. Fiorini, A. Longoni, Optimized readout methods of silicon drift detectors for high-resolution X-ray spectroscopy. Nucl. Instrum. Methods. Phys. Res. A **568**, 336–342 (2006)
28. R. Fitzgerald, K. Keil, K.F.J. Heinrich, Science **159**, 528–530 (1968)
29. B.L. Doyle, D.S. Walsh, P.G. Kotula, P. Rossi, T. Schulein, M. Rohde, X-Ray Spectrom. **34**, 279–284 (2005)
30. P.G. Kotula, J.R. Michael, M. Rohde, Microsc. Microanal. Suppl. **2**(14), 116–117 (2008)
31. P.G. Kotula, M.R. Keenan, Application of multivariate statistical analysis to STEM X-ray spectral images: interfacial analysis in microelectronics. Microsc. Microanal. **12**(6), 538–544 (2006)
32. M.R. Keenan, P.G. Kotula, Accounting noise in the multivariate statistical analysis of TOF-SIMS data. Surf. Interf. Anal. **36**, 203–212 (2004)
33. M.R. Keenan, P.G. Kotula, Optimal scaling of ToF-SIMS spectrum-images prior to multivariate statistical analysis. Appl. Surf. Sci. **231–232**, 240–244 (2004)
34. M.R. Keenan, P.G. Kotula, Apparatus and System for Multivariate Spectral Analysis. US Patent # 6,584,413, 2003
35. M.R. Keenan, P.G. Kotula, Method of Multivariate Spectral Analysis. US Patent # 6,675,106, 2004
36. M.R. Keenan, Multivariate analysis of spectral images composed of count data. in *Techniques and Applications of Hyperspectral Image Analysis*, ed. by H. Grahn, P. Geladi (Wiley & Sons, Chinchester, 2007)
37. I.T. Jollife, *Principal Component Analysis*, 2nd edn. (Springer, New York, 2002)
38. H.F. Kaiser, The varimax criterion for analytic rotation in factor analysis. Psychometrika **23**(3), 187–200 (1958)
39. M.R. Keenan, Exploiting spatial-domain simplicity in spectral image analysis. Surf. Int. Anal. **41**, 79–87 (2009)
40. S.V. Prasad, J.R. Michael, T.R. Christenson, EBSD studies on wear-induced subsurface regions in LIGA nickel. Scripta Mater. **48**, 255–260 (2003)
41. S.V. Prasad, T.W. Scharf, P.G. Kotula, J.R. Michael, T.R. Christenson, J Microelectromech. Syst. **18**, 695 (2009)
42. S.V. Prasad, C.C. Battaile, P.G. Kotula, Scripta Mater. **64**, 729–732 (2011)
43. T.W. Scharf, P.G. Kotula, S.V. Prasad, Acta Materiala **58**, 4100–4109 (2010)